Research Article Vol. 5, No. 4 / April 2018 / Optica 382

Localization of light in an optical microcapillary induced by a droplet

Tabassom Hamidfar,[1,2] Kirill V. Tokmakov,[1] Brian J. Mangan,[3] Robert S. Windeler,[3] Artemiy V. Dmitriev,[1,4] Dashiell L. P. Vitullo,[1] Pablo Bianucci,[2] and Michael Sumetsky[1,*]

[1]Aston Institute of Photonic Technologies, Aston University, Birmingham B4 7ET, UK
[2]Concordia University, Montreal, Québec H4B 1R6, Canada
[3]OFS Laboratories, 19 Schoolhouse Road, Somerset, New Jersey 08873, USA
[4]School of Physics and Astronomy and Institute of Gravitational Wave Astronomy, University of Birmingham, Birmingham B15 2TT, UK
*Corresponding author: m.sumetsky@aston.ac.uk

Received 7 December 2017; revised 16 February 2018; accepted 24 February 2018 (Doc. ID 315289); published 29 March 2018

Sensing with optical whispering gallery modes (WGMs) is a rapidly developing detection method in modern microfluidics research. This method explores the perturbations of spectra of WGMs propagating along the wall of an optical microcapillary to characterize the liquid medium inside it. Here we show that WGMs in a silica microcapillary can be fully localized (rather than perturbed) by evanescent coupling to a water droplet and, thus, form a high-quality-factor microresonator. The spectra of this resonator, measured with a microfiber translated along the capillary, present a hierarchy of resonances that allow us to determine the size of the droplet and variation of its length due to the evaporation. The resolution of our measurements of this variation equal to 4.5 nm is only limited by the resolution of the optical spectrum analyzer used. The discovered phenomenon of complete localization of light in liquid-filled optical microcapillaries suggests a new type of microfluidic photonic device as well as an ultraprecise method for microfluidic characterization.

OCIS codes: (140.3945) Microcavities; (230.3990) Micro-optical devices; (060.2340) Fiber optics components; (060.2370) Fiber optics sensors.
https://doi.org/10.1364/OPTICA.5.000382

1. INTRODUCTION

Research and development of optical whispering gallery mode (WGM) microresonators has grown significantly over the last several decades, finding applications in telecommunications [1–4], fabrication of microlasers [5–9], quantum electrodynamics [10,11], quantum networks [12,13], microfluidics [14–17], optomechanics [18,19], and other fields of science and engineering. These microresonators are usually fabricated in the form of spheres, toroids, bottles, bubbles, cylinders, disks, and capillaries (see e.g., Refs [1,2,10,14,20]).

Similar to the acoustic WGMs discovered by Lord Rayleigh more than 100 years ago [21], optical WGMs propagate very close to the surface of optical microresonators. This fact has both positive and negative consequences for applications. On the one hand, since WGMs are isolated from the microresonator core, thermal and electrical tuning devices can be included into interior part of the microresonator without degrading its quality factor [22,23]. Of special interest is the development of microfluidic optomechanics based on liquid-filled microcapillaries, which is also based on the effect of isolation of WGMs from the liquid inside the resonator [24].

Alternatively, coupling between WGMs and the interior of the microresonator is critical for the development of ultraprecise capillary microfluidic sensors [14,17,25,26]. To this end, researchers fabricate optical microcapillaries having very narrow (a few microns thick) walls, which allow WGMs to evanescently penetrate through the internal capillary surface and probe the interior medium. It is expected that these microfluidic sensors, similar to WGM microresonators sensing the environment at their peripheral surface [16], can achieve breakthrough single-molecule sensitivity.

Light propagating in the form of a WGM along an optical fiber surface can be fully controlled by the exceptionally small nanoscale variation of the effective fiber radius [27]. In particular, the deformation of a fiber by just a fraction of a nanometer can completely localize WGMs and form a high-quality-factor microresonator [28]. This means that the fiber radius variation sufficient for governing WGMs can be dramatically smaller than the wavelength of light. The technological platform based on this phenomenon—surface nanoscale axial photonics (SNAP)—demonstrates the fabrication of miniature resonant optical devices at the fiber surface with unprecedented sub-angstrom precision and ultralow loss [3,27,29].

The success of the work presented below is primarily based on the idea of bridging the SNAP platform [27] and WGM microfluidic sensing platform [25], which have much in common [30]. In fact, while SNAP considers WGMs controlled by nanoscale deformation of the *outer surface* of an optical fiber, similar control can be performed in microcapillaries by small and slowly varying *internal nonuniformities*. Recently we showed that the introduction of SNAP resonators is possible by deformation of the external as well as the internal capillary surfaces [31]. Alternatively, here we consider liquid situated in a *uniform* microcapillary. We show that the control over the WGMs propagating along the microcapillary can be performed only by the nonuniformities of the liquid. In particular, we demonstrate that a water droplet situated inside a silica microcapillary can fully localize WGMs and introduce a high-quality-factor optical microresonator. Our discovery paves the way for the development of a novel comprehensive method for microfluidic sensing and a new type of tunable resonant microfluidic-based photonic devices.

2. OBSERVATION OF AN OPTICAL MICRORESONATOR INDUCED BY A DROPLET

The microcapillary used in our experiment was prepared from a polymer-coated silica capillary fiber drawn at OFS Laboratories. Figure 1(a) shows the optical microscope image of the cross section of this capillary after the polymer coating was removed in hot sulfuric acid. From this image, the external and internal radii of the capillary were determined as $r_{\text{int}} = 61$ μm and $r_{\text{ext}} = 68$ μm. In our experiment, one end of a several-centimeters-long fiber was glued in into the needle of a syringe that was used to launch and position the water droplets inside the fiber. The other end was left open. The silica microcapillary was prepared by removing the coating from a few-centimeter section in the middle of this fiber.

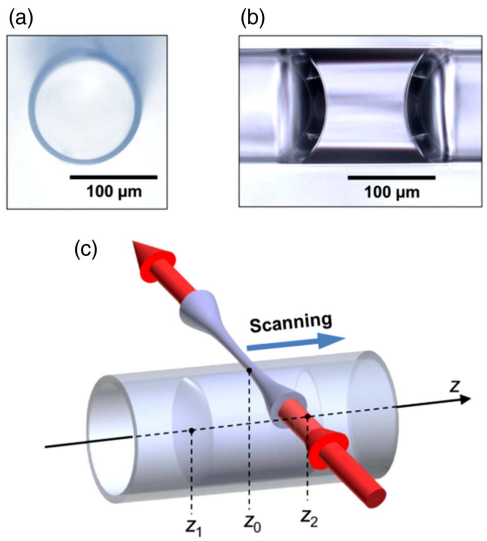

Fig. 1. (a) The optical microscope image of the cross section of the silica microcapillary used in the experiment. This image was used to determine the radius of the capillary and the thickness of its wall. (b) The optical microscope image of a water droplet inside the capillary. The droplet meniscuses caused by the surface tension are clearly seen. (c) Illustration of the experiment. The input-output taper with a micron-diameter waist (microfiber) is positioned normally to the capillary. The microfiber excites WGMs which propagate along the microcapillary wall and sense the droplet.

An optical microscope image of a sample droplet positioned inside the stripped section of the fiber is shown in Fig. 1(b). It is seen that the droplet possesses the characteristic meniscuses introduced by the surface tension.

The idea of our experiment is illustrated in Fig. 1(c). A biconical fiber taper with a micron-diameter waist (3-mm-length microfiber with diameter of 1.6 μm) was oriented normal to the capillary and connected to the LUNA optical spectrum analyzer (1.3 pm wavelength resolution). The microfiber was translated along the capillary axis z and periodically placed in direct mechanical contact with the capillary to measure the transmission power $P(z, \lambda)$ as a function of the microfiber coordinate along the capillary z and wavelength λ [27]. Figure 2(a) shows the surface plot of transmission spectra $P(z, \lambda)$ collected in the bandwidth 1539.5 nm $< \lambda <$ 1545 nm at points spaced by 2 μm along the 600-μm capillary section with the droplet in the middle. The spectra are found to be quasiperiodic in wavelength with a period of 3.92 nm (see Supplement 1). The time of each measurement (including the time required for recording the spectrum and the time of translation of the microfiber between the measurement points) was 10 s. Consequently, the full time of recording of the spectra along the 600-μm capillary section was 50 min, while the measurements along the length of the droplet took around 11 min.

The spectral plot in Fig. 2(a) clearly outlines the area where the water droplet is situated. As explained in the next section, the green pathways (dips) outside the droplet area correspond to the cutoff wavelengths of WGMs. Some of these pathways (e.g., those close to 1540.2 nm, 1540.9 nm, and 1541.8 nm) cross the droplet area unaffected. This means that the corresponding WGMs are not perturbed by the presence of the droplet. Other lines (e.g., those close to 1539.9 nm, 1540.5 nm, and 1543.3 nm) are interrupted in the droplet area, indicating that the corresponding WGMs are perturbed by the droplet. The interruption of these lines is accompanied by the appearance of additional resonances, which is explained by the full localization of the corresponding WGMs in the droplet area. The evanescent coupling of these WGMs to the water droplet causes the positive shifts of their cutoff wavelengths and the formation of a high-quality-factor microresonator. The position of resonances is in excellent agreement with the theory presented below.

3. THEORY OF CUTOFF WAVELENGTHS AND QUANTIZATION OF SLOW WGMS

High-quality-factor optical resonance lines are commonly observed in the WGM spectra of optical fibers [14,25–27]. These resonances correspond to the so-called cutoff wavelengths of light λ_{mp}. Here m and p are the azimuthal and radial quantum numbers, which numerate modes propagating in an axially symmetric and uniform fiber (in particular, a capillary fiber). The expression for the electromagnetic field of these modes is factorized in the cylindrical coordinates (z, ρ, φ) as [32]

$$E^{\pm}_{mp}(z, \rho, \varphi) = \exp(\pm i\beta_{mp}(\lambda)z)\exp(im\varphi)Q_{mp}(\rho).$$

Here $\beta_{mp}(\lambda)$ is the propagation constant, and the function $Q_{mp}(\rho)$ exponentially decreases outside the capillary for $\rho > r_{\text{ext}}$ and inside the capillary for $\rho < r_{\text{int}}$. The optical modes of our interest are the WGMs, which are adjacent to the optical fiber surface. At cutoff wavelengths λ_{mp}, the propagation constants of these modes approach zero, $\beta_{mp}(\lambda_{mp}) = 0$. The speed of propagation of WGMs with small $\beta_{mp}(\lambda)$ along the capillary axis

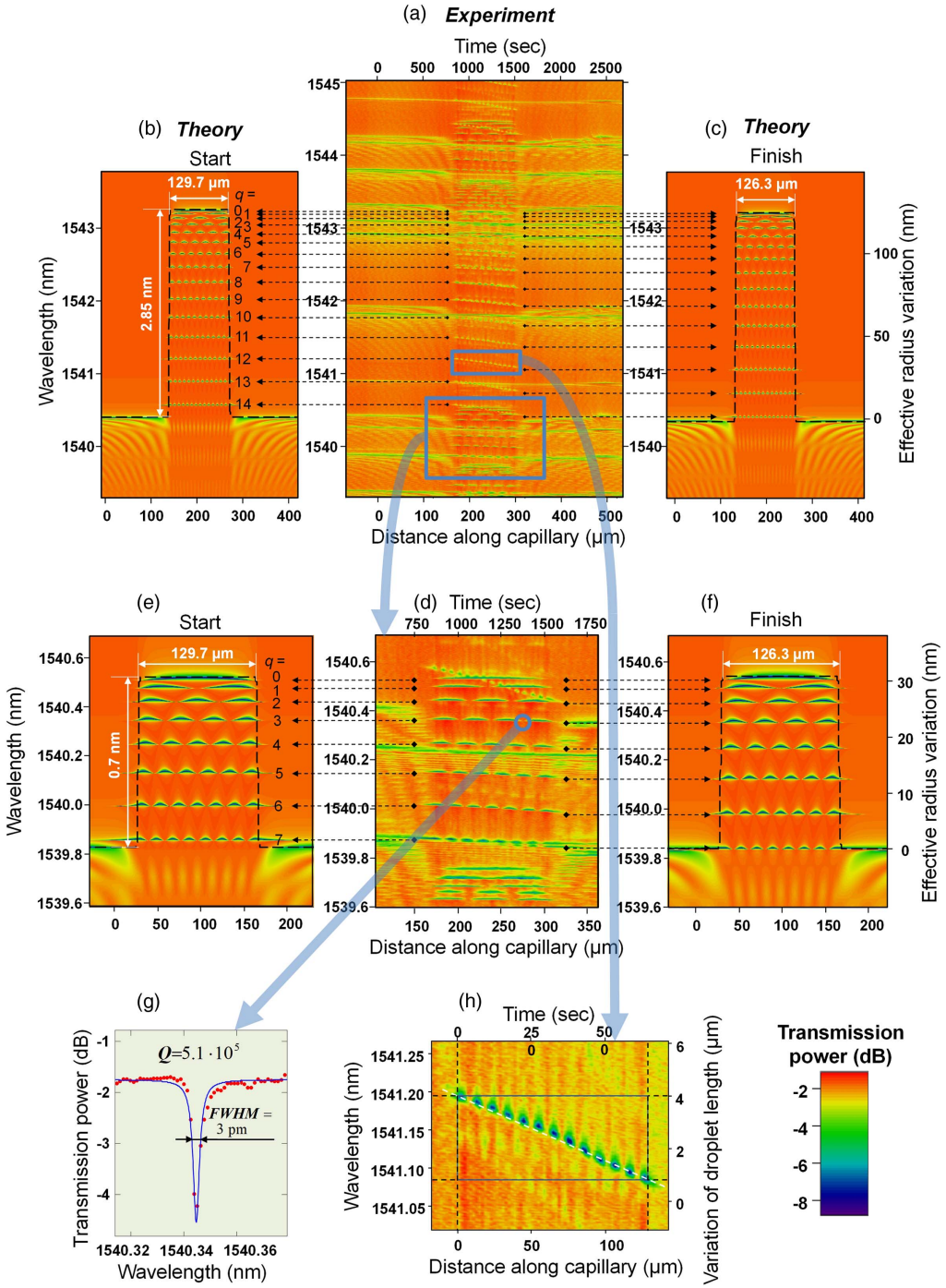

Fig. 2. Surface plot of the transmission power spectra collected by the input-output microfiber translated along the microcapillary with a droplet inside. The spectral (vertical axis) and spatial (horizontal axis) resolutions of the scan were 1.3 pm and 2 μm, respectively. The central part of the plot indicates the region where the droplet was situated. (b) and (c) Surface plots of the calculated transmission power spectra corresponding to the stationary droplet with the initial (b) and final (c) dimensions which were obtained for a single cutoff wavelength using Eqs. (1)–(3). The initial and final dimensions were taken from the experimental plot (a) at axial coordinates z_1 and z_2 [Fig. 1(c)] when the measurement of the droplet region started and finished. (d)–(f) Magnified spectral region of the surface plot (a) and the theoretical models of the droplet similar to those shown in (b) and (c) but for a different cutoff wavelength. (g) The resonance of the droplet-induced microresonator measured at the node indicated at the spectral plot (d). (h) Magnified spectral region of the surface plot (a) containing the pathway of resonances with the axial quantum number $q = 12$ which was used for the analysis of the droplet evaporation.

is slow. It is due to the slowness of WGMs that they can be governed by angstrom-scale variations of the effective fiber radius employed in SNAP [27]. As explained below, a similar effective radius variation effect can be introduced by the shifts of cutoff wavelengths λ_{mp} caused by the evanescent coupling of WGMs to a water droplet inside a capillary fiber.

Figure 3(a) shows the dependencies of λ_{mp} for the silica microcapillary with the refractive index $n_{\text{cap}} = 1.46$ and external radius

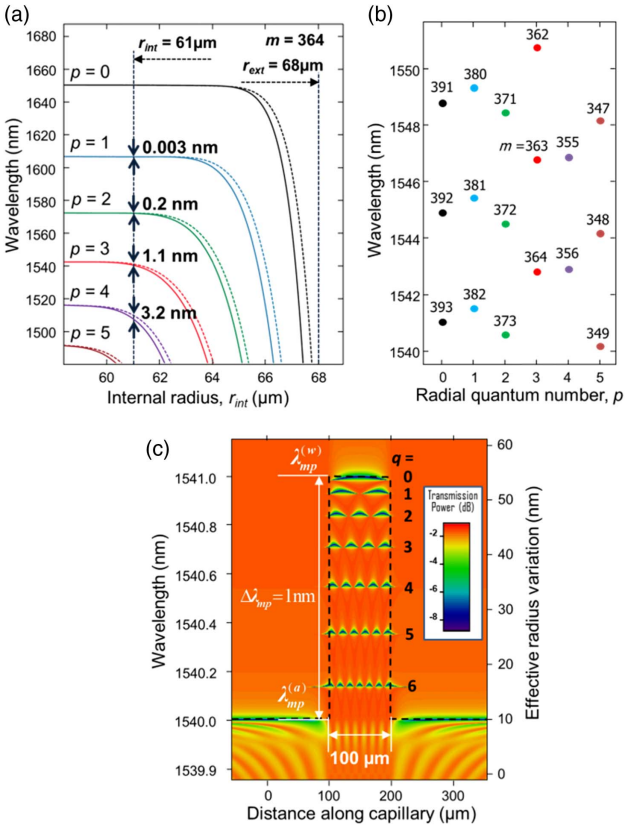

Fig. 3. (a) Cutoff wavelengths with the azimuthal quantum number $m = 364$ and radial quantum numbers $p = 0, 1, 2, 3, 4, 5$ for the silica microcapillary with external radius $r_{ext} = 68$ μm as a function of the microcapillary internal radius r_{int}. The solid and dashed curves correspond to the empty and water-filled microcapillary, respectively. (b) The distribution of cutoff wavelengths (dots) for the TE-polarized WGMs having $p = 0, 1, 2, 3, 4, 5$ in the bandwidth 1540 nm $< \lambda <$ 1550 nm. The corresponding azimuthal quantum numbers m are shown next to each of the dots. (c) A sample surface plot of transmission power spectra calculated using Eqs. (1)–(3) for the water-induced shift of the cutoff wavelength equal to 1 nm and microfiber-capillary coupling parameters indicated in the text.

$r_{ext} = 68$ μm as a function of internal radius r_{int}. The solid and dashed curves correspond to the empty and water-filled capillary, respectively. The external and internal radii, $r_{int} = 61$ μm and $r_{ext} = 68$ μm, of the capillary used in our experiment are indicated by the vertical dashed lines. In calculations, we chose the azimuthal quantum number $m = 364$ so that the cutoff wavelength of the first WGM sensitive to water corresponds to the wavelength ~1.54 μm close to the value of an experimental cutoff wavelength in Fig. 2(a). The noticeable shifts caused by the presence of water are found for the WGMs with radial quantum numbers $p \geq 2$. Specifically, for $p = 2, 3, 4$, and 5 these shifts are 0.003 nm, 0.2 nm, 1.1 nm, 3.2 nm, and 6.0 nm, respectively. The characteristic behavior of evanescent field in the water-filled microcapillary can be found, e.g., in [25].

Figure 3(b) shows the calculated cutoff wavelengths λ_{mp} for the transverse-electric (TE)-polarized WGMs with radial quantum numbers $p = 0, 1, \ldots, 5$, which are situated in the bandwidth 1.54 μm $< \lambda <$ 1.55 μm (see Supplement 1). As we found above, the WGMs having frequencies λ_{mp} with small $p = 0$ and 1 are not affected by liquid. On the other hand, the WGMs with large $p \gg 1$, which strongly scatter from interfaces, may be undetectable due to their high attenuation. For this reason, the values λ_{mp} situated in the bandwidth 1.54 μm $< \lambda <$ 1.55 μm are shown in Fig. 3(b) for quantum numbers $p \leq 5$, which are presumably detected in our experiment. The corresponding azimuthal quantum numbers m ranging from 347 to 393 are shown in Fig. 3(b) as well. The cutoff wavelengths of the transverse-magnetic (TM)-polarized WGMs, which are not shown in this figure, are known to have significantly smaller quality-factors than those of the TE-polarized WGMs due to scattering from the surface and bulk nonuniformities [33]. The distribution of the cutoff wavelengths in Fig. 3(b) is in a reasonable quantitative agreement with that of the measured resonant wavelengths in Fig. 2(a).

The appearance of a microresonator induced by a water droplet is explained as follows. In the vicinity of cutoff wavelengths, the propagation constant is small and can be determined in the first order of the perturbation theory as (see Supplement 1),

$$\beta_{mp}^{(a),(w)}(\lambda) = 2^{3/2}\pi n_{\text{cap}}(\lambda_{mp}^{(a),(w)})^{-3/2}(\lambda_{mp}^{(a),(w)} - \lambda)^{1/2}, \quad (1)$$

where n_{cap} is the refractive index of the capillary material and superscript indices $^{(a)}$ and $^{(w)}$ correspond to the air-filled and water-filled capillaries, respectively. From Eq. (1), the propagation constant is real for wavelengths $\lambda < \lambda_{mp}^{(a),(w)}$ and pure imaginary for $\lambda > \lambda_{mp}^{(a),(w)}$. Assume that the cutoff wavelength $\lambda_{mp}^{(a)}$ of the empty capillary experiences a relatively small positive perturbation and becomes equal to $\lambda_{mp}^{(w)}$ after the capillary is filled in with water. Then, for the wavelength λ, which is close to $\lambda_{mp}^{(a)}$ and $\lambda_{mp}^{(w)}$, the expressions for propagation constants in the water-filled and empty capillary can be calculated from Eq. (1). In our approximation, the relatively small perturbation of the WGM dependence on the radial coordinate in $Q_{mp}(\rho)$ due to the presence of water can be neglected. Then, the behavior of WGMs along the microcapillary with a droplet inside is determined by the one-dimensional wave equation,

$$\frac{d^2\Psi_{mp}}{dz^2} + \beta_{mp}^2(\lambda, z)\Psi_{mp} = 0, \quad (2)$$

where $\beta_{mp}(z, \lambda) = \beta_{mp}^{(w)}(\lambda)$ inside the droplet region, $z_1 < z < z_2$ [Fig. 1(c)], and $\beta_{mp}(z, \lambda) = \beta_{mp}^{(a)}(\lambda)$ outside it. Substitution of expressions for the propagation constants from Eq. (1) into Eq. (2) makes Eq. (2) equivalent to the Schrödinger equation for the rectangular quantum well [34]. In particular, it becomes obvious that WGMs with wavelengths $\lambda_{mp}^{(a)} < \lambda < \lambda_{mp}^{(w)}$ can be localized by the droplet. These modes are oscillatory in the droplet region (here $\beta_{mp}(\lambda, z)$ is real) and exponentially decay outside it (here $\beta_{mp}(\lambda, z)$ is pure imaginary). The quantization rule for these modes is similar to the quantization rule for the rectangular quantum well. The transmission amplitude through the microfiber placed in contact with the capillary at point z is expressed through the Green's function of Eq. (2), $G(z, z, \lambda)$ as [35]

$$A(z, \lambda) = A_0 - \frac{i|C|^2 G(z, z, \lambda)}{1 + DG(z, z, \lambda)}. \quad (3)$$

Here constants A_0, $|C|$, and D are the microfiber–capillary coupling parameters, which are usually determined experimentally. As an example, Fig. 3(c) shows the surface plot of the transmission power $P(z, \lambda) = |A(z, \lambda)|^2$ for our microcapillary having $r_{int} = 61$ μm and $r_{ext} = 68$ μm with a water droplet of 100 μm length inside. The transmission power $P(z, \lambda)$ shown

in Fig. 3(c) is found for the characteristic microfiber–capillary coupling parameters $A_0 = 0.8 - 0.1i$, $|C|^2 = 0.02\ \mu m^{-1}$, and $D = 0.02 + 0.025i\ \mu m^{-1}$ [35]. The cutoff wavelength of the empty capillary is set to $\lambda_{mp}^{(a)} = 1540$ nm, close to one of the cutoff wavelengths observed in our experiment [Fig. 2(a)]. Approximating the behavior of the $p = 3$ cutoff wavelength in Fig. 3(a), we assume that this wavelength increases by $\Delta\lambda_{mp} = 1$ nm and becomes $\lambda_{mp}^{(w)} = 1.541\ \mu m$ in the droplet region. The introduced cutoff wavelength profile [bold black dashed line in Fig. 3(c)] corresponds to a quantum well in Eq. (2) and, equivalently, to an optical microresonator. The right-hand-side vertical axis in Fig. 3(c) is the effective radius variation determined from the cutoff wavelength variation by the rescaling equation $\Delta r_{mp}/r_{ext} = \Delta\lambda_{mp}/\lambda_{mp}^{(a)}$. The horizontal resonance pathways in Fig. 3(c) with interchanging nodes and antinodes correspond to the axial eigenvalues of this microresonator with quantum numbers $q = 0, 1, \ldots 6$. In analogy to the bottle microresonators induced by the external radius variation [27], this microresonator can be called a *droplet-induced bottle microresonator*.

4. INTERPRETATION OF THE EXPERIMENTAL OBSERVATIONS

The surface plot of experimental spectra in Fig. 2(a) exhibit several series of resonance pathways. Some of pathways cross the droplet region without visible perturbation. As explained above, they correspond to the cutoff wavelengths with small radial quantum numbers $p < 2$. Other pathways experience a break in the droplet region, which is accompanied by the appearance of series of resonance lines with interchanging nodes and antinodes. The behavior of each of these series, taken separately, is similar to that in the numerical example of a droplet-induced bottle resonator shown in Fig. 3(c). To clarify this, we consider two examples. The first example corresponds to the behavior of the cutoff wavelength which is close to 1540.44 nm outside the droplet. This wavelength experiences the positive shift of 2.85 nm in the region of the droplet. The shift introduces a microresonator containing 15 eigenvalues with axial quantum numbers $q = 0, 1, \ldots, 14$ indicated on the theoretical 2D plots of transmission power in Figs. 2(b) and 2(c) described below. Based on calculations shown in Fig. 3(a), we suggest that the radial quantum number of these eigenvalues is equal to $p = 4$. As noted above, the process of characterization of the microresonator region took around 11 min. During this time the droplet became smaller in length due to evaporation. It is well known from quantum mechanics that the decrease of the length of the rectangular quantum well (resonator) leads to the growth of the separation between its eigenvalues [34]. For this reason, the pathways indicating the axial eigenvalues in Fig. 2(a) have a small negative slope. As shown in the next section, the measurement of this slope allows us to detect the variation of the droplet size with nanometer precision. Figures 2(b) and 2(c) show the results of our theoretical characterization of the droplet using Eqs. (1)–(3), which fit the experimental spectra before and after measurements (see Supplement 1). The theoretical as well as experimental pathways with axial quantum numbers q indicated in Fig. 2(b) consist of $q + 1$ antinodes. The agreement between the positions of wavelength resonances found theoretically and their positions found experimentally is excellent. In the second example, we consider a 2D spectral fragment magnified in Fig. 2(d). Here the cutoff wavelength equal to 1539.88 nm outside the droplet is shifted by 0.7 to 1540.58 nm in the droplet region. Based on calculations presented in Fig. 3(a), we suggest that the radial quantum number of this cutoff wavelength is $p = 3$. Our numerical modelling shown in Figs. 2(e) and 2(f) precisely confirms the length of the droplet L equal to 129.7 and 126.3 μm before and after its characterization, which has been initially calculated in the first example. Finally, Fig. 2(g) shows that the quality factor of the induced microresonator is remarkably large, $\sim 5 \cdot 10^5$.

Before the full stabilization of the droplet, it was translated along the originally dry capillary from right to left. As the result, tiny micro-islands of water adjacent to the internal capillary surface were left behind at the right-hand-side of the droplet. Examination of resonance pathways outside the droplet in Fig. 2(a) allows us to distinguish between the perturbations caused by outside contamination, which disturbs all pathways similarly, and perturbations caused by the water islands situated inside the capillary. As discussed above, the latter disturb the pathways with relatively large radial quantum numbers p and have negligible effect on pathways with $p < 2$. For example, the pathway close to $\lambda = 1540.9$ nm, which crosses the droplet unperturbed and presumably has $p = 0$, is straight everywhere except the disturbance near $z = 500\ \mu m$. Since this disturbance is replicated in all other pathways, we suggest that it is caused by perturbations of the external capillary surface. However, the pathway close to $\lambda = 1540.5$ nm is straight at the left hand of the droplet and, unlike the pathway at $\lambda = 1540.9$ nm, is corrugated at its right-hand side. For this reason, we suggest that these corrugations are caused by water islands inside the capillary.

5. EVAPORATION OF THE DROPLET AND CONCOMITANT EFFECTS

Due to the evaporation of the droplet in the process of its characterization, the successive measurements comprising the 2D plot in Fig. 2(a) present the spectra of the microresonator continuously reducing in length. For this reason, in contrast to the purely horizontal resonance pathways in theoretical plots in Figs. 2(b), 2(c), 2(e), and 2(f), the resonance pathways in the droplet region of experimental Fig. 2(a) are tilted. Analysis of the behavior of these tilted pathways allows us to determine the variation of the droplet length with exceptionally accurate nanometer precision. Figure 2(h) shows the magnified fraction of the 2D plot in Fig. 2(a), which includes the resonance pathway corresponding to axial quantum number $q = 12$ consisting of 13 antinodes. The most accurate measurement of the immediate wavelength eigenvalue of the microresonator is achieved at the nodes of this pathway, which correspond to the minimum coupling between the excited WGM and input-output microfiber. For the model of the rectangular quantum well described by Eqs. (1) and (2), the change ΔL of the resonator length L can be determined from the shift $\Delta\lambda$ of the eigenvalue λ_{mpq} with large axial quantum number $q \gg 1$ by the equation

$$\Delta L = \frac{4n_{cap}^2 L^3}{q^2 \lambda_{mp}^3} \Delta\lambda \tag{4}$$

derived in Supplement 1. From this equation and analysis of the pathway with axial quantum number $q = 12$ shown in Fig. 2(h), we find that the total wavelength shift $\Delta\lambda_t = 0.11$ nm, which the eigenvalue $\lambda_{mp,12} \approx 1.541\ \mu m$ acquires during the time of scan of the droplet region equal to 10.7 min, corresponds to the

droplet reduction in length of $\Delta L_t = 3.8$ μm and shrinking speed of 0.35 μm/min. Using Eq. (4), the resolution of the measurement of the droplet length variation is found from the resolution of our optical spectrum analyzer equal to $\Delta\lambda_r = 0.13$ pm as $\Delta L_r = 4.5$ nm. Due to geometric reasons, this remarkably high resolution is, nevertheless, two orders of magnitude worse than that achieved in SNAP technology for the effective variation of the optical fiber radius [3,27,29].

It is interesting to estimate the deformation of the capillary due to the surface tension induced by the droplet. The additional pressure P experienced by the capillary wall can be estimated by the Young–Laplace equation, $P = 2\gamma/R$ [36]. Assuming the characteristic value of the surface tension $\gamma \sim 0.1$ N/m and capillary and meniscus radii $r_{\text{ext}} \sim R \sim 100$ μm, we find $P \sim 1$ kPa. Depending on the actual values of the surface tension at the water–air, water–silica, and silica–air interfaces, which usually have the same order of magnitude [36], this pressure can be positive or negative. Consequently, it can increase or decrease the effective radius of the capillary. The radius variation δr caused by the surface pressure can be found from the elasticity theory of thin-walled cylinders as $\delta r = P r_{\text{ext}}^2 (E\Delta r)^{-1}$, where Δr is the capillary wall thickness and E is its Young modulus [37]. Since the effect of the stress-induced refractive index variation is usually smaller than that of the mechanical deformation, we estimate the corresponding shift of the capillary radius as $\delta r \sim 3$ pm and the cutoff wavelength as $\delta\lambda \sim \delta r\lambda/r_{\text{ext}} \sim \lambda_{mp}\gamma(E\Delta r)^{-1} \sim 0.1$ pm. These values are much smaller than those observed in our experiment for WGMs with radial quantum numbers $p > 2$. We suggest that the introduced shift can be detected by more accurate measurements of the cutoff wavelength shifts of WGMs with $p = 0$ since their evanescent coupling to the droplet is negligibly small.

Usually, a water droplet carries an electric charge e (see e.g., Refs. [38,39]). The value of e is limited by the maximum charge-induced expanding force, which can be withheld by the surface tension. Estimating e by the Rayleigh formula for a spherical droplet, $e \le 8\pi(\varepsilon_0\gamma)^{1/2}R_0^{3/2}$, where ε_0 is the vacuum permittivity and $R_0 \sim 100$ μm is the characteristic radius of the droplet, we find $e \le 2 \cdot 10^{-11}$ C. Assuming that the distribution of charge along the droplet surface is uniform, we find that the charge-induced effective radius variation of the capillary (limited by the droplet stability) has the same order of magnitude as the radius variation induced by the surface tension calculated above. However, the electrostatic calculations (see e.g., [40]) show that the distribution of charge at the droplet–capillary surface interface can be strongly nonuniform. The charge density can grow by an order of magnitude near the droplet edges where the introduced capillary radius variation can be significantly greater.

Another effect induced by the droplet charge is the DC Kerr effect [41,42]. By modelling the droplet as a cylinder of length L and charge e, we estimate the electric field inside the capillary as $E = e/(2\pi\varepsilon_0 n_{\text{cap}} L r_{\text{ext}})$. For $e \sim 10^{-11}$ C, $L \sim 100$ μm and $r_{\text{ext}} \sim 50$ μm, we have $E \sim 10^7$ V/m. The refractive index variation introduced by this field is expressed through the third-order electric susceptibility $\chi^{(3)}$ as $\delta n_{\text{DCKerr}} = (3\chi^{(3)}/2n_{\text{cap}})E^2$ [42]. For silica, $\chi^{(3)} \sim 2 \cdot 10^{-22}$ m^2/V^2 and the refractive index variation of the capillary introduced by the DC Kerr effect in the droplet region is estimated as $\delta n_{\text{DCKerr}} \sim 10^{-7}$. This corresponds to the cutoff wavelength shift of $\delta\lambda \sim \delta n_{\text{DCKerr}}\lambda_{mp}/n_{\text{cap}} \sim 0.1$ pm having the same order of magnitude as the shifts introduced by the surface tension mechanically. From the above expressions for E and δn_{DCKerr}, we have $\delta n_{\text{DCKerr}} \sim L^{-2}$. Therefore, the DC Kerr effect can be increased by an order of magnitude for a droplet with three times smaller length. In addition, the DC Kerr effect, being proportional to the local charge density squared, is significantly greater near the droplet edges where, as noted above, the charge density maximizes.

6. DISCUSSION

We have shown, experimentally and theoretically, that a droplet positioned inside an optical microcapillary can trap the WGMs propagating along the capillary wall and localize them completely. The evanescent tails of WGMs penetrate into a thin layer of the droplet through the internal capillary surface. Consequently, the WGMs spectra characterize the medium, which is adjacent to the interface between the droplet and the capillary. In contrast to previous WGM microfluidic sensing methods [14–17], the presence of the droplet-induced microresonator allows us to monitor the droplet dynamics nonlocally with the fixed position of the input-output microfiber. For example, the resonance spacing measured at a single point z_0 in the droplet region [Fig. 1(c)] allowed us to determine the immediate length of the droplet, which changed in the process of evaporation. More generally, examination of the WGM spectra measured at one or a few points along the droplet enables monitoring the behavior of the droplet away from these points. The important question remained is whether the collected spectral data is sufficient to solve the inverse problem completely and determine the refractive index variation near the internal capillary surface.

The future research and development exploring the discovered phenomenon promises wide-ranging applications in microfluidics, surface science, and microphotonics. It is of great interest to apply the developed method to investigate the droplets of different liquids, simple and complex, including colloidal liquids [36]. As an example, the immediate positions and velocities of an individual and, presumably, a few micro/nanoparticles in a colloidal liquid can be determined from the dynamics of WGM spectrum measured at a fixed microfiber position. In contrast to the SNAP microfluidic sensor [30,31], the microresonator enabling this nonlocal characterization of the droplet is naturally introduced and does not have to be fabricated.

It is expected that the size of particles that can be detected and monitored with our approach can achieve sub-nanoscale dimensions. In fact, it has been shown that a WGM microsphere resonator sensor enriched with plasmonic nanoparticles can detect single atoms [15]. Due to the analogy between the behavior of evanescent WGM at the periphery of a microsphere and at the interior of a capillary, we suggest that the similar resolution is feasible for plasmon-enhanced WGM sensing inside a microcapillary. Remarkably, our method potentially enables the detection of the immediate axial coordinate of moving nanoparticles and molecules, which was not possible in the previous approaches. More complex phenomena at the solid–liquid interfaces can be investigated [43–46].

Funding. Royal Society (WM130110); Horizon 2020 Framework Programme (H2020) (H2020-EU.1.3.3, 691011); Engineering and Physical Sciences Research Council (EPSRC) (EP/P006183/1).

Acknowledgment. M. S. acknowledges the Royal Society Wolfson Research Merit Award.

See Supplement 1 for supporting content.

REFERENCES

1. A. B. Matsko, *Practical Applications of Microresonators in Optics and Photonics* (CRC Press, 2009).
2. G. C. Righini, Y. Dumeige, P. Féron, M. Ferrari, G. Nunzi Conti, D. Ristic, and S. Soria, "Whispering gallery mode microresonators: fundamentals and applications," Riv. Nuovo Cimento Soc. Ital. Fis. **34**, 435–488 (2011).
3. M. Sumetsky, "Delay of light in an optical bottle resonator with nanoscale radius variation: dispersionless, broadband, and low loss," Phys. Rev. Lett. **111**, 163901 (2013).
4. W. Liang, D. Eliyahu, V. S. Ilchenko, A. A. Savchenkov, A. B. Matsko, D. Seidel, and L. Maleki, "High spectral purity Kerr frequency comb radio frequency photonic oscillator," Nat. Commun. **6**, 7957 (2015).
5. M. Cai, O. Painter, K. J. Vahala, and P. C. Sercel, "Fiber-coupled microsphere laser," Opt. Lett. **25**, 1430–1432 (2000).
6. S. Yakunin, L. Protesescu, F. Krieg, M. I. Bodnarchuk, G. Nedelcu, M. Humer, G. De Luca, M. Fiebig, W. Heiss, and M. V. Kovalenko, "Low-threshold amplified spontaneous emission and lasing from colloidal nanocrystals of caesium lead halide perovskites," Nat. Commun. **6**, 8056 (2015).
7. J. M. Ward, Y. Yang, and S. Nic Chormaic, "Glass-on-glass fabrication of bottle-shaped tunable microlasers and their applications," Sci. Rep. **6**, 25152 (2016).
8. F. X. Gu, F. M. Xie, X. Lin, S. Y. Linghu, W. Fang, H. Zeng, L. Tong, and S. Zhuang, "Single whispering-gallery-mode lasing in polymer bottle microresonators via spatial pump engineering," Light Sci. Appl. **6**, e17061 (2017).
9. M. Humar, A. Dobravec, X. Zhao, and S. H. Yun, "Biomaterial microlasers implantable in the cornea, skin, and blood," Optica **4**, 1080–1085 (2017).
10. K. J. Vahala, "Optical microcavities," Nature **424**, 839–846 (2003).
11. J. Volz, M. Scheucher, C. Junge, and A. Rauschenbeutel, "Nonlinear π phase shift for single fiber-guided photons interacting with a single resonator-enhanced atom," Nat. Photonics **8**, 965–970 (2014).
12. H. J. Kimble, "The quantum internet," Nature **453**, 1023–1030 (2008).
13. A. Reiserer, "Cavity-based quantum networks with single atoms and optical photons," Rev. Mod. Phys. **87**, 1379–1418 (2015).
14. X. Fan and I. M. White, "Optofluidic microsystems for chemical and biological analysis," Nat. Photonics **5**, 591–597 (2011).
15. M. D. Baaske and F. Vollmer, "Optical observation of single atomic ions interacting with plasmonic nanorods in aqueous solution," Nat. Photonics **10**, 733–739 (2016).
16. E. Kim, M. D. Baaske, and F. Vollmer, "Towards next-generation label-free biosensors: recent advances in whispering gallery mode sensors," Lab Chip **17**, 1190–1205 (2017).
17. T. Reynolds, N. Riesen, A. Meldrum, X. Fan, J. M. M. Hall, T. M. Monro, and A. Francois, "Fluorescent and lasing whispering gallery mode microresonators for sensing applications," Laser Photon. Rev. **11**, 1600265 (2017).
18. M. Aspelmeyer, T. J. Kippenberg, and F. Marquardt, "Cavity optomechanics," Rev. Mod. Phys. **86**, 1391–1452 (2014).
19. R. Dahan, L. L. Martin, and T. Carmon, "Droplet optomechanics," Optica **3**, 175–178 (2016).
20. M. Sumetsky, "Lasing microbottles," Light Sci. Appl. **6**, e171022017 (2017).
21. L. Rayleigh, "The problem of the whispering gallery," Sci. Pap. **5**, 617–620 (1912).
22. B. Peng, K. Ozdemir, S. Rotter, H. Yilmaz, M. Liertzer, F. Monifi, C. M. Bender, F. Nori, and L. Yang, "Loss-induced suppression and revival of lasing," Science **346**, 328–332 (2014).
23. A. V. Dmitriev and M. Sumetsky, "Tunable photonic elements at the surface of an optical fiber with piezoelectric core," Opt. Lett. **41**, 2165–2168 (2016).
24. G. Bahl, K. H. Kim, W. Lee, J. Liu, X. Fan, and T. Carmon, "Cavity optomechanics on a microfluidic resonator with water and viscous liquids," Nat. Commun. **4**, 1994 (2013).
25. I. M. White, H. Oveys, and X. Fan, "Liquid-core optical ring-resonator sensors," Opt. Lett. **31**, 1319–1321 (2006).
26. V. Zamora, A. Díez, M. V. Andrés, and B. Gimeno, "Refractometric sensor based on whispering-gallery modes of thin capillaries," Opt. Express **15**, 12011–12016 (2007).
27. M. Sumetsky, "Nanophotonics of optical fibers," Nanophotonics **2**, 393–406 (2013).
28. M. Sumetsky and J. M. Fini, "Surface nanoscale axial photonics," Opt. Express **19**, 26470–26485 (2011).
29. N. A. Toropov and M. Sumetsky, "Permanent matching of coupled optical bottle resonators with better than 0.16 GHz precision," Opt. Lett. **41**, 2278–2281 (2016).
30. M. Sumetsky, "Slow light optofluidics: a proposal," Opt. Lett. **39**, 5578–5581 (2014).
31. T. Hamidfar, A. Dmitriev, B. Mangan, P. Bianucci, and M. Sumetsky, "Surface nanoscale axial photonics at a capillary fiber," Opt. Lett. **42**, 3060–3063 (2017).
32. A. W. Snyder and J. Love, *Optical Waveguide Theory* (Chapman and Hall, 1983).
33. M. L. Gorodetsky, A. D. Pryamikov, and V. S. Ilchenko, "Rayleigh scattering in high-Q microspheres," J. Opt. Soc. Am. B **17**, 1051–1057 (2000).
34. S. Flügge, *Practical Quantum Mechanics* (Springer, 1971), vol. **1**.
35. M. Sumetsky, "Theory of SNAP devices: basic equations and comparison with the experiment," Opt. Express **20**, 22537–22554 (2012).
36. J. C. Berg, *An Introduction to Interfaces and Colloids: The Bridge to Nanoscience* (World Scientific, 2009).
37. S. P. Timoshenko and J. N. Goodier, *Theory of Elasticity*, 3rd ed. (McGraw-Hill, 1970).
38. L. P. Santos, T. R. D. Ducati, L. B. S. Balestrin, and F. Galembeck, "Water with excess electric charge," J. Phys. Chem. C **115**, 11226–11232 (2011).
39. S. H. Behrens and D. G. Grier, "The charge of glass and silica surfaces," J. Chem. Phys. **115**, 6716–6721 (2001).
40. R. W. Scharstein, "Capacitance of a tube," J. Electrost. **65**, 21–29 (2007).
41. N. Mukherjee, R. A. Myers, and S. R. J. Brueck, "Dynamics of second-harmonic generation in fused silica," J. Opt. Soc. Am. B **11**, 665–669 (1994).
42. A. Liu, M. Digonnet, and G. Kino, "DC Kerr coefficient in silica: theory and experiment," Proc. SPIE **3542**, 102–107 (1994).
43. J. D. Tice, H. Song, A. D. Lyon, and R. F. Ismagilov, "Formation of droplets and mixing in multiphase microfluidics at low values of the Reynolds and the capillary numbers," Langmuir **19**, 9127–9133 (2003).
44. D. Lis, E. H. G. Backus, J. Hunger, S. H. Parekh, and M. Bonn, "Liquid flow along a solid surface reversibly alters interfacial chemistry," Science **344**, 1138–1142 (2014).
45. C. Hao, J. Li, Y. Liu, X. Zhou, Y. Liu, R. Liu, L. Che, W. Zhou, D. Sun, L. Li, L. Xu, and Z. Wang, "Superhydrophobic-like tunable droplet bouncing on slippery liquid interfaces," Nat. Commun. **6**, 7986 (2015).
46. O. Björneholm, M. H. Hansen, A. Hodgson, L. M. Liu, D. T. Limmer, A. Michaelides, P. Pedevilla, J. Rossmeisl, H. Shen, G. Tocci, E. Tyrode, M. M. Walz, J. Werner, and H. Bluhm, "Water at interfaces," Chem. Rev. **116**, 7698–7726 (2016).